JOURNAL OF GUIDANCE, CONTROL, AND DYNAMICS
Vol. 30, No. 5, September–October 2007

Three-Dimensional Ascent Trajectory Optimization for Stratospheric Airship Platforms in the Jet Stream

Sangjong Lee*
Korea Aerospace Research Institute, Daejeon 305-333, Republic of Korea
and
Hyochoong Bang†
Korea Advanced Institute of Science and Technology, Daejeon 305-701, Republic of Korea

DOI: 10.2514/1.27344

Full three-dimensional optimal-ascent trajectory design is addressed for a stratospheric airship platform, considering real jet stream and flight constraints. The target airship's equations of motion are first constructed by including wind effects and its inherent features such as added mass and buoyancy effects. For realistic trajectory optimization, additional necessary modeling of the jet stream, aerodynamic force, and thrust are established based on a flight test, wind-tunnel test, and meteorological observation data. In addition, detailed path constraints such as the target airship's performance and local airspace are also accounted for. The sequential quadratic programming approach is employed as a numerical solver for both minimum flight time and minimum-energy performance indices. The solutions obtained satisfy all of the constraints and are largely affected by the jet stream of high wind speed. From the optimization results, the minimum flight time trajectory is recommended due to the low flight performance of the airship in contrast to its huge size and heavy weight.

Nomenclature

$\boldsymbol{A}$	=	aerodynamic force vector
$\boldsymbol{B}$	=	buoyancy vector
B/W	=	buoyancy-to-weight ratio
$\boldsymbol{C}_E$, $\boldsymbol{C}_I$	=	equality and inequality constraint vectors during optimization
C_L, C_D	=	aerodynamic lift and drag coefficients
e	=	error of terminal position and angle constraints
$\boldsymbol{F}$	=	external force vector
f, φ	=	nonlinear function
$\boldsymbol{G}$	=	gravity vector
h	=	altitude
J, $\bar{J}$	=	performance index
k	=	time index during optimization
$\mathbf{M}_a$	=	added mass tensor
m_{ax}, m_{ay}, m_{az}	=	added mass
m_T	=	total mass of the airship
$\boldsymbol{p}$	=	unknown design parameter vector
q	=	dynamic pressure of freestream
$\boldsymbol{T}$	=	thrust vector
T	=	thrust
Tr	=	throttle
t	=	time
V	=	relative flight speed
$\boldsymbol{V}$, $\boldsymbol{V}_I$	=	relative and inertial flight speed vector
Vol	=	envelope volume of the airship
W	=	total weight of the airship
$\boldsymbol{W}_I$	=	jet stream speed vector in the inertial frame
w_E, w_N	=	east and north components of the jet stream speed
$\dot{w}_{wx}$, $\dot{w}_{wy}$, $\dot{w}_{wz}$	=	wind variation components in the wind-axes coordinate system
$\boldsymbol{x}$, $\boldsymbol{u}$	=	state and control vectors
x_h, y_h, z_h	=	local-level coordinate system
x_i, y_i, z_i	=	Earth-fixed inertial coordinate system
x_w, y_w, z_w	=	relative wind-axes coordinate system
α	=	angle of attack
γ	=	relative flight path angle
$\boldsymbol{\Theta}$	=	discretized unknown parameter vector during optimization
ξ, η	=	weighting of time and energy in the performance index
ρ_a, ρ_h	=	density of surrounding air and helium
ϕ	=	bank angle
$\boldsymbol{\Psi}_E$, $\boldsymbol{\Psi}_I$, $\boldsymbol{\Upsilon}$	=	equality, inequality, and path constraint vectors in the continuous system
ψ	=	relative heading angle
ψ_w	=	heading angle of the jet stream
$\boldsymbol{\omega}_w$	=	angular rate of the wind-axes frame with regard to the Earth-fixed frame

I. Introduction

THE stratospheric airship platform (SAP) is being considered as a new platform that will provide satellitelike missions such as telecommunication, broadcasting relays, environmental observations, and surveillance at the stratospheric altitude. The staion-keeping flight is an airship's unique feature, in contrast to a fixed-wing aircraft. Compared with geostationary and low-Earth-orbit satellites, it can ensure long endurance at the geostationary position near the surface of the Earth with minimal operation cost. This capability can lead to a more efficient flight for high-resolution images and surveying information. On the other hand, the airship has lower flight performance in flight speed, rate of climb, and stiffness of the structure; consequently, the lighter-than-air (LTA) vehicles are critically affected by the environment conditions such as the fast wind present at high altitude. Also, the SAP should not violate the airspace of the neighboring countries while climbing to the stratospheric altitude. Therefore, constructing an optimal trajectory

Received 17 August 2006; revision received 2 January 2007; accepted for publication 5 January 2007.

*Senior Researcher, Air Vehicle System Department, Aircraft Division; albert@kari.re.kr.

†Associate Professor, Division of Aerospace Engineering; hcbang@fdcl.kaist.ac.kr. Senior Member AIAA.

Fig. 1 Midaltitude unmanned airship (VIA-50).

for the SAP and satisfying various constraints is gaining more emphasis than ever.

Several countries are currently developing SAPs, and Korea also launched the SAP program in 2002. The concept evaluation demonstrator of a 50-m unmanned airship was developed in the first phase, with the flight test completed successfully in 2005. The second phase is ongoing, and conceptual design and feasibility studies are currently being conducted. Colozza [1] and Eguchi and Yokomaku [2] surveyed the present level of necessary technologies for developing SAPs, and characterized some design parameters such as the efficiency and specific power of the regenerative fuel cell (RFC) and solar array.

Over the past few decades, a considerable number of studies were conducted on trajectory optimization of fixed-wing aircraft and reentry launch vehicles. However, only a few attempts were made thus far in the field of airship trajectory optimization problems. Bestaoui and Hamel [3] and Hima and Bestaoui [4] conducted several studies focusing on a very small blimp (length of 6 m and maximum flight altitude of 200 m). Although they obtained reference trajectories, there seem to be limitations:

1) The trajectory is assumed to be a helix with constant curvature and torsion.

2) The blimp dynamics are not fully reflected, because only trimmed flight conditions are considered, and the differential equations are simplified as nonlinear algebraic equations with no aerodynamic forces and no control surface moments.

3) The differential equation is simplified on the assumption that the body and wind axes coincide with each other.

Zhao et al. [5] was first concerned with the trajectory optimization of a high-altitude airship (HAA). A point-mass model of an airship was used, which includes the effect of wind profiles. The numerical solutions were consistent with the approximated analytical solutions under simplified assumptions. Though the results are significant in the area of an airship's optimal trajectory generation, they also suffer from some limitations:

1) The simple flight conditions assumes neutral buoyancy (the airship's weight equals the buoyancy), so that the net lift force becomes zero.

2) Angle of attack, sideslip angle, and roll angle are considered zero with constant thrust. The two restrictions cannot describe the whole flight envelope of the SAP.

3) The simple flight scenario starts from an initial altitude of 18 km and reaches an operating altitude of 21.5 km. It is well known that the wind (or jet stream) velocity is most severe around the altitude of 10–15 km, and so the full history of the flight trajectory from the ground cannot be easily demonstrated.

To overcome such limitations, full point-mass equations of motion for the airship are treated in this paper by considering wind effects, added mass, and buoyancy effects. Furthermore, an accurate modeling of the dynamics is developed based on wind-tunnel test results, flight test, computational fluid dynamics analysis, and meteorological observation data. The real constraints of flight conditions and airship performance are included so that the optimal trajectories reflect the realistic conditions to the best extent possible.

The main objective of this study is to design optimal and efficient SAP trajectories for reaching the stratospheric altitude from the ground under various hard constraints. A target SAP model is a 200-m-long stratospheric unmanned airship (VIA-200), and its necessary geometric and performance data for the trajectory optimization problem are based on the output of conceptual design. The resulting two-point boundary-value problem can only be solved numerically [6]. To obtain a numerical solution, a direct shooting method is used. In other words, the trajectory optimization problem is converted into a parameter optimization problem, such as in [7]. It is solved by modifying the CFSQP code [8] for the sequential quadratic programming (SQP) algorithm.

This paper is organized as follows. The dynamic equations of a SAP motion and the conceptual design information of the target SAP are introduced first in Sec. II. Necessary mathematical modeling of the external forces, added mass, and jet stream are defined in Sec. III. Section IV discusses constraints to be satisfied during the optimization process, which are mainly related to the performance of the target airship. By using such modeling and constraints, the three-dimensional optimal trajectories for minimum flight time and minimum energy are presented in Sec. V.

II. Flight Dynamics of a Stratospheric Airship

A. Stratospheric Airship

Korea is one of the challengers in the field of stratospheric airship and has launched the SAP program. The conceptual evaluation phase was completed successfully in 2005 after the flight test of a 50-m unmanned midaltitude airship (VIA-50), shown in Fig. 1. Several core technologies should be applied and implemented for developing the SAP, that is, hybrid propulsion system, high stiffness, and lightweight materials. One of the most promising systems for the hybrid power source is to combine the RFC with solar arrays. In the daytime, power can be obtained from the solar energy, and the redundant energy is stored up. Conversely, the fuel cell system is used to produce main power by a combination of hydrogen and oxygen during the nighttime, and the accumulated energy would be used for breaking apart water into its constituent elements, hydrogen and oxygen, through the electrolyzer.

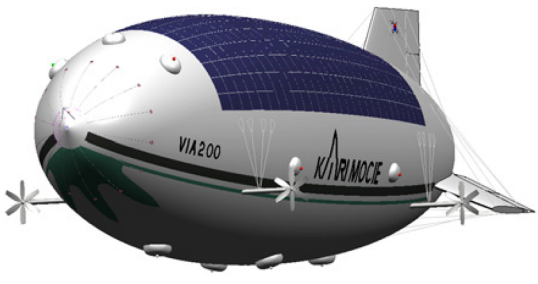

Fig. 2 Stratospheric airship platform (VIA-200).

First, a feasible sizing study for the target SAP model (VIA-200), shown in Fig. 2, was conducted through an iterative sizing program developed by [9]. For this work, the necessary input parameters were selected, referring to the feasibility studies in [1,2]. It is assumed that the maximum flight speed of the target SAP is designed as 20 m/s at the mission altitude of 20 km, to overcome 12 m/s of jet stream and to stay at its desired location. The buoyancy-to-weight ratio is 0.97 and its pressure altitude is 24 km. As a result of the conceptual sizing, the target SAP's length is 200 m, its volume is 265, 746 m^3 with a weight of 21,726 kg, and the maximum available power for thrust is 100 kW. VIA-200's design parameters and outputs are summarized in Tables 1 and 2, respectively. The final design output data are used for constructing the optimal trajectories.

B. Flight Dynamics of an Airship

The general dynamic equations of a SAP are derived for flight over the flat and nonrotating Earth, considering buoyancy, added mass, and relevant conceptual design data of the VIA-200. To include the effect of the jet stream as a moving wind field, the dynamic equations of motion can be derived in the relative wind-axes [10], inertial wind-axes [11], or body-axes [12] coordinate systems. The relative wind-axes system is more convenient than other coordinate systems, as discussed by Miele et al. [10], because it expresses the wind-effect terms explicitly, bringing easier understanding. In this paper, the relative wind-axes frame is adopted as the reference coordinate system, and two-dimensional vertical plane motion [10,11] is extended to the three-dimensional plane based on [10,13].

The coordinate system is presented in Fig. 3. $Ox_iy_iz_i$ is an Earth-fixed inertial frame (I frame), with the origin on the surface of the Earth. $Px_hy_hz_h$ is the local-level frame (h frame), with the origin at the mass center of the airship. These two frames are aligned with each other, and the x_i axis points north, the y_i axis points east, and the z_i axis points down. The last coordinate system is the relative wind-axes frame (w frame) of $Px_wy_wz_w$, for which the x_w axis is commonly aligned with the relative flight speed of the airship. The local-level and wind-axes frames can be transformed to each other by the following transformation matrix in Eq. (1), in terms of three angular parameters [13]:

$$C_h^w = \begin{bmatrix} \cos\gamma\cos\psi & \cos\gamma\sin\psi & -\sin\gamma \\ \sin\phi\sin\gamma\cos\psi - \cos\phi\sin\psi & \sin\phi\sin\gamma\sin\psi + \cos\phi\cos\psi & \sin\phi\sin\gamma \\ \cos\phi\sin\gamma\cos\psi + \sin\phi\sin\psi & \cos\phi\sin\gamma\sin\psi - \sin\phi\cos\psi & \cos\phi\cos\gamma \end{bmatrix} \tag{1}$$

Table 1 Input parameters for conceptual design of the VIA-200

Design parameters	Value
Maximum flight speed, m/s	20
Mission (staion-keeping) altitude, km	24
Pressure altitude, km	24
Drag coefficient, C_D	0.04
Fitness ratio	4.0
Buoyancy-to-weight ratio	0.97
Night hours, h	13.4
Estimated weight of structure, kg	1500
Estimated weight of propulsive system, kg	1500
Estimated weight of onboard system, kg	500
Specific weight of envelope materials, kg/m^2	0.2
Specific weight of solar array, kg/m^2	0.6
Specific energy of RFC, W · h/kg	450
Specific energy of solar array, g/W	3.69
Required power of payload, kW	10
Required power of onboard system, kW	30
Efficiency of RFC	0.53
Efficiency of electric motor	0.9
Efficiency of electric propeller	0.7
Efficiency of dc-to-dc converter	0.8

Table 2 Conceptual design results of the VIA-200

Output design parameters	Value
Length, m	200
Envelope volume, m^3	265,746
Hull Area, m^2	25,564
Area of solar array, m^2	4417
Buoyancy, kg	21,074
Maximum take-off weight, kg	21,726
Weight of envelope, kg	6385
Weight of RFC, kg	8429
Weight of solar array, kg	2650
Available power of thrust, kW	100
Available power of RFC, kWh/kg	3793
Available power of solar array, kW	507
Available power of supplement system, kW	150

The inertial velocity of the airship is the vector sum of the relative wind and the relative flight speed, as shown in Fig. 3. Let $\boldsymbol{i}_h$, $\boldsymbol{j}_h$, and $\boldsymbol{k}_h$ be the unit vectors along the local-level frame of $Px_hy_hz_h$, and let $\boldsymbol{i}_w$, $\boldsymbol{j}_w$, and $\boldsymbol{k}_w$ be the unit vectors along the wind-axes frame of $Px_wy_wz_w$. The relative flight speed vector can then be expressed as

$$\boldsymbol{V} = \boldsymbol{V}_I - \boldsymbol{W}_I = (\dot{x}_i - w_N)\boldsymbol{i}_h + (\dot{y}_i - w_E)\boldsymbol{j}_h - \dot{h}\boldsymbol{k}_h \tag{2}$$

The relative flight speed can be represented in the local-level frame using Eq. (1):

$$\boldsymbol{V}|_I = \left(C_h^w\right)^T \cdot V\boldsymbol{i}_w = V\cos\gamma\cos\psi\boldsymbol{i}_h + V\cos\gamma\sin\psi\boldsymbol{j}_h - V\sin\gamma\boldsymbol{k}_h \tag{3}$$

Finally, the three-dimensional kinematic equations are summarized as Eq. (4) by comparing Eqs. (2) and (3):

$$\frac{\mathrm{d}x_i}{\mathrm{d}t} = \dot{x}_i = V\cos\gamma\cos\psi + w_N$$
$$\frac{\mathrm{d}y_i}{\mathrm{d}t} = \dot{y}_i = V\cos\gamma\sin\psi + w_E, \qquad \frac{\mathrm{d}h}{\mathrm{d}t} = \dot{h} = V\sin\gamma \tag{4}$$

By Newton's second law, the force equilibrium equation in the inertial frame is expressed as

$$\boldsymbol{F} = m_T\boldsymbol{a} = m_T\left.\frac{\mathrm{d}\boldsymbol{V}_I}{\mathrm{d}t}\right|_I \quad \text{with} \quad m_T = m + m_{ax} + m_{ay} + m_{az} \tag{5}$$

where m_T includes the empty mass m and the added masses, m_{ax}, m_{ay}, and m_{az}. When a body moves through fluid, it must push some mass of fluid out of the way. If the body is accelerated, the surrounding fluid must also be accelerated. Under this circumstance, the body behaves as if it were heavier, such that mass is added [14]. This is the most unique characteristic of an airship, which is generally inflated with a large amount of helium.

Because the relative wind-axes frame is taken as a reference frame, the absolute acceleration should be described in the wind-axes frame after taking time derivative of the absolute velocity of Eq. (2):

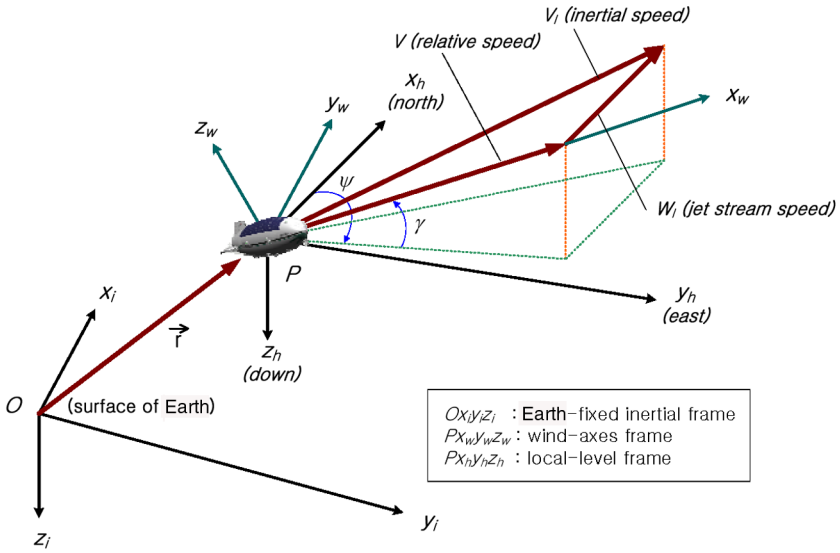

Fig. 3 Definition of the coordinate system.

$$\left.\frac{\mathrm{d}\boldsymbol{V}_I}{\mathrm{d}t}\right|_I = \left.\frac{\mathrm{d}\boldsymbol{V}}{\mathrm{d}t}\right|_I + \left.\frac{\mathrm{d}\boldsymbol{W}_I}{\mathrm{d}t}\right|_I = \left.\frac{\mathrm{d}\boldsymbol{V}}{\mathrm{d}t}\right|_w + \boldsymbol{\omega}_w \times \boldsymbol{V}|_w + C_h^w \left.\frac{\mathrm{d}\boldsymbol{W}_I}{\mathrm{d}t}\right|_I \tag{6}$$

where $\boldsymbol{\omega}_w$ satisfies

$$\boldsymbol{\omega}_w = \begin{bmatrix} p_w \\ q_w \\ r_w \end{bmatrix} = \begin{bmatrix} 1 & 0 & -\sin\gamma \\ 0 & \cos\phi & \sin\phi\cos\gamma \\ 0 & -\sin\phi & \cos\phi\cos\gamma \end{bmatrix} \begin{bmatrix} \dot{\phi} \\ \dot{\gamma} \\ \dot{\psi} \end{bmatrix} \quad \text{and}$$
$$\left.\frac{\mathrm{d}\mathbf{W}_I}{\mathrm{d}t}\right|_w = \begin{bmatrix} \dot{w}_{wx} \\ \dot{w}_{wy} \\ \dot{w}_{wz} \end{bmatrix} = C_h^w \left.\frac{\mathrm{d}\mathbf{W}_I}{\mathrm{d}t}\right|_I = C_h^w \begin{bmatrix} \dot{w}_N \\ \dot{w}_E \\ 0 \end{bmatrix} \tag{7}$$

The external forces consist of the buoyancy force, thrust, aerodynamic force, and gravity force. The gravity force is always in the direction of the unit vector $\boldsymbol{k}_h$ and opposite to the buoyancy force direction. All of the external forces should be expressed in the wind-axes coordinate system. Thus,

$$\begin{aligned} \boldsymbol{G} + \boldsymbol{B} &= C_h^w(mg - B)\boldsymbol{k}_h, \\ \boldsymbol{T} + \boldsymbol{A} &= [T\cos(\mu+\alpha) - D]\boldsymbol{i}_w - [T\sin(\mu+\alpha) + L]\boldsymbol{k}_w \end{aligned} \tag{8}$$

where μ represents the tilting angle of the propellers installed on both sides of the VIA-200.

Combining Eqs. (6) and (7) with Eq. (8) leads to the final representation of Eq. (5) in the wind-axes frame, after several algebraic manipulations. Finally, solving the simultaneous algebraic equations for the derivatives $\dot{V}$, $\dot{\gamma}$, and $\dot{\psi}$, the force equilibrium equations can be represented as

$$\begin{aligned} \dot{V} &= \frac{(T\cos\alpha - D) - (mg - B)\sin\gamma}{m_T} - \dot{w}_{wx} \\ \dot{\gamma} &= \frac{(T\sin\alpha + L)\cos\phi - (mg - B)\cos\gamma}{m_T V} \\ &\quad + \frac{\dot{w}_{wz}\cos\phi + \dot{w}_{wy}\sin\phi}{V} \\ \dot{\psi} &= \frac{(T\sin\alpha + L)\sin\phi}{m_T V\cos\gamma} + \frac{\dot{w}_{wz}\sin\phi - \dot{w}_{wy}\cos\phi}{V\cos\gamma} \end{aligned} \tag{9}$$

where

$$\begin{aligned} \dot{w}_{wx} &= \dot{w}_N\cos\gamma\cos\psi + \dot{w}_E\cos\gamma\sin\psi \\ \dot{w}_{wy} &= \dot{w}_N(\sin\phi\sin\gamma\cos\psi - \cos\phi\sin\psi) + \dot{w}_E(\sin\phi\sin\gamma\sin\psi \\ &\quad + \cos\phi\cos\psi) \\ \dot{w}_{wz} &= \dot{w}_N(\cos\phi\sin\gamma\cos\psi + \sin\phi\sin\psi) + \dot{w}_E(\cos\phi\sin\gamma\sin\psi \\ &\quad - \sin\phi\cos\psi) \end{aligned}$$

III. Modeling of the Airship Supplement System

A. Aerodynamic Forces Modeling

The aerodynamic forces are obtained from the aerodynamic database compiled from a wind-tunnel test using a 1/25-scale mock-up of the VIA-50 model. The aerodynamic database was updated through flight tests and additional computational fluid dynamics (CFD) analysis. The aerodynamic database of the VIA-50, shown in Fig. 4, can be extended to the VIA-200 [15]. The lift and moment coefficients are not affected by the difference in Reynolds number if the geometries of the airships are identical. However, the drag coefficient critically depends on the varying Reynolds number. The Reynolds number of the VIA-200 ($Re = 8.0 \times 10^6$) is only half of that of the VIA-50 ($Re = 17.2 \times 10^6$) at the mission altitude. This region is part of the fully turbulent areas, because the range of Reynolds number between 10^5 and 10^6 corresponds to a critical transient region from laminar to turbulent flow. In a fully turbulent region, the drag coefficient shows a slight decrease as the Reynolds number increases. However, its variation is small enough to be ignored [16]. Furthermore, CFD analysis for the VIA-50 and VIA-200 do not show much difference. Therefore, aerodynamic coefficients of the VIA-50 can be suitably applied to the VIA-200. Using the wind-tunnel test data and CFD analysis, the aerodynamic coefficients of lift and drag can be approximated as functions of the angle of attack by fourth-order polynomials, with their curves shown in Fig. 4:

$$\begin{aligned} C_L(\alpha) &= 0.5903\alpha^4 + 1.2231\alpha^3 - 0.3248\alpha^2 + 0.9211\alpha + 0.0118 \\ C_D(\alpha) &= 0.340\alpha^4 + 0.0662\alpha^3 + 1.2248\alpha^2 + 0.0334\alpha + 0.040 \end{aligned} \tag{10}$$

The lift and drag force can be calculated by

$$L = q \cdot \mathrm{Vol}^{2/3} \cdot C_L, \qquad D = q \cdot \mathrm{Vol}^{2/3} \cdot C_D \tag{11}$$

B. Thrust Modeling

The maximum flight speed for the VIA-200 is designed at 20 m/s at the mission altitude of 20 km, and corresponding maximum

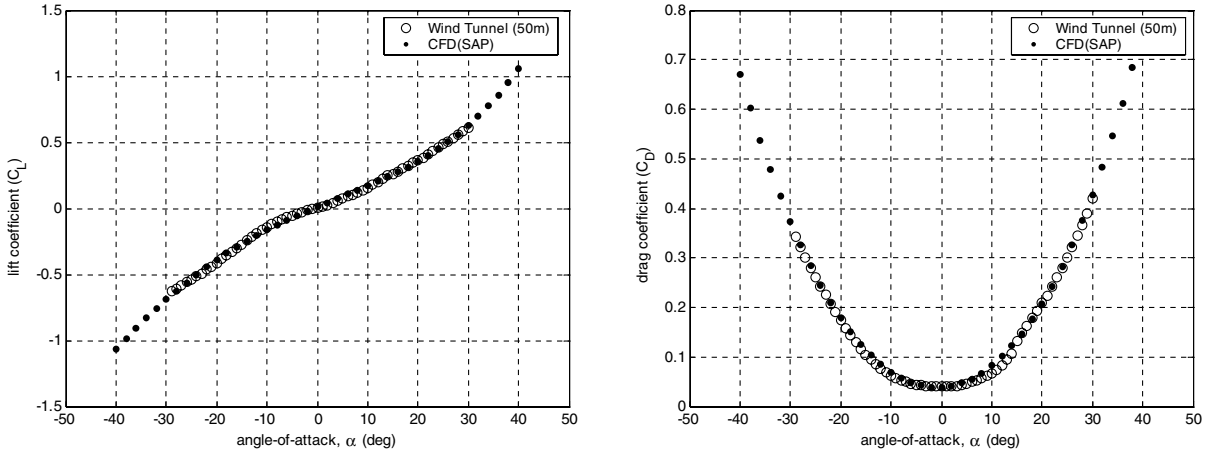

Fig. 4 Aerodynamic coefficients for the VIA-200.

available power of the propulsion system is 100 kW, as shown in Table 2. To reach this flight speed, the required thrust and power are given by [1]

$$T_{\text{req}} = q \cdot \text{Vol}^{2/3} \cdot C_D, \qquad P_{\text{req}} = \frac{T \cdot V}{\eta_p \cdot \eta_m} \tag{12}$$

where η_p and η_m represent the efficiency of the propellers and electric motor equipped in the VIA-200. The values 0.7 and 0.9 are used for the efficiencies, respectively. With regard to the regenerative fuel cell system, the lower air density at high altitude does not lead to a reduction in power. Assuming that the equipped regenerative fuel cell system and the solar array with enough capacity supply the required power continuously, the maximum flight speed, corresponding thrust, and angle of attack can be calculated from the trimmed conditions. The numerical approach is used to calculate these values under the given flight conditions for an altitude from 0 to 26 km and flight path angle from −10 to 10 deg. Thus, the thrust profile can be modeled as a function of h and γ. Figure 5 summarizes the thrust and its modeling result. A two-dimensional interpolation routine is adopted to compute the corresponding thrust during the optimization process. Finally, to expedite the convergence of the optimization process, thrust is converted as a function of a Tr, ranging from 0 to 1.0.

C. Added Mass and Buoyancy Modeling

Added mass effect arises from the airship mass being in the same order of magnitude as the mass of displaced air. To date, the relevant research works [3,17,18] employed the standard methods based on the original formulation by Lamb [19], which fits the hull shape with an ellipsoid of revolution. This method ignored the effect of horizontal and vertical tail fins and the gondola of airships. This paper takes the added mass term determined from CFD analysis by considering the geometry design of the SAP to include the effect of both tail fins and gondola [20]. An added mass tensor is calculated from the CFD analysis and its effects due to tail fins and gondola show 20% increase for pitch and yaw axes, compared with the results for the ellipsoid of revolution model [20]. The diagonal terms of the added mass tensor are the main terms for the body axes of airships, respectively, for m_{ax}, m_{ay}, and m_{az} of Eq. (5). Because it is assumed that the air density varies in a unit with operating altitude, the values should be multiplied by the corresponding density to obtain the added mass in the optimization process:

$$\mathbf{M}_a = \begin{bmatrix} 2.1391 \times 10^4 & 1.6502 \times 10^{-12} & 1.3365 \times 10^{-11} \\ -2.0890 \times 10^{-12} & 2.4363 \times 10^5 & 9.8516 \times 10^1 \\ -2.2134 \times 10^{-12} & -9.8516 \times 10^1 & 2.4363 \times 10^5 \end{bmatrix} (\text{m}^3) \tag{13}$$

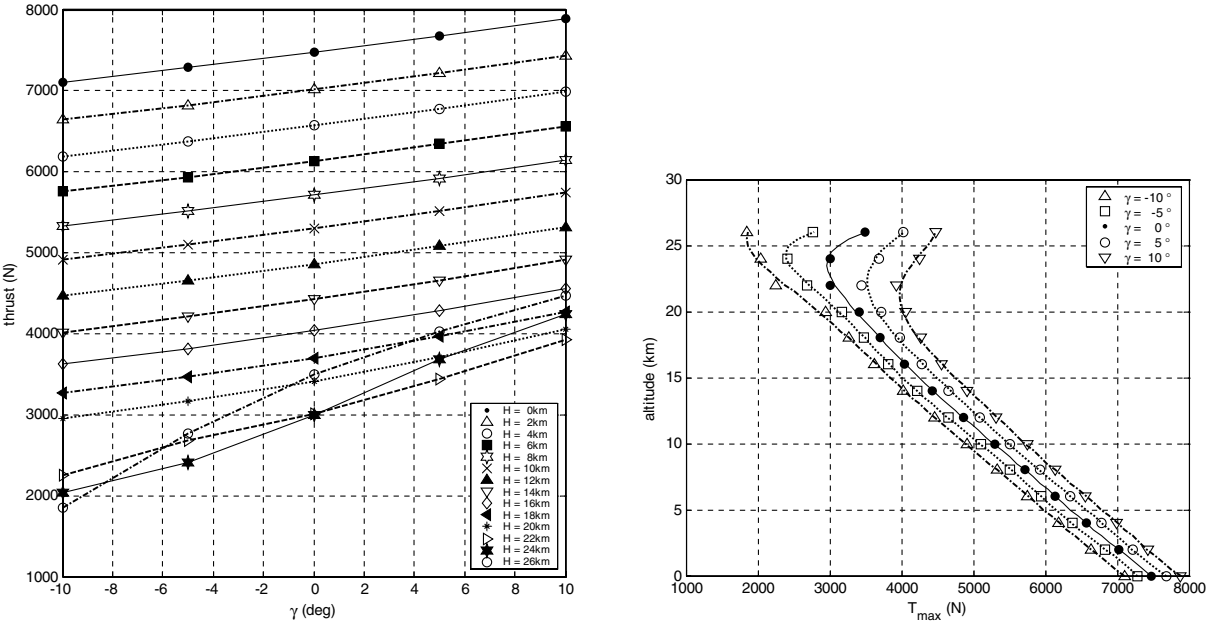

Fig. 5 Thrust modeling for the VIA-200.

The buoyancy force is another typical discriminator between LTA vehicles and conventional aircraft. It plays the role of lifting airships upward and is equal to the weight of displaced air by its volume immersed in the atmosphere. The net lift that can be available for payload, system, and structure is determined by subtracting the weight of the lift gas and envelope [14]:

$$L_{\text{net}} = B - W = \text{Vol}(\rho_a - \rho_h)g - W_{\text{env}} \quad \text{with} \quad B = \text{Vol} \cdot \rho_a \cdot g \tag{14}$$

where ρ_a and ρ_h refer to the density of the surrounding atmosphere and helium, respectively. For the helium that is generally used as the lifting gas, the gross lift per unit volume $(\rho_a - \rho_h)g$ is 10.359 N/m^3. As the airship ascends, the helium and air density fall with decreasing pressure, but the occupied volume of the helium increases at the same ratio. Conversely, falling temperature tends to increase the density, but reduce the volume, so that the two effects are canceled out again [14]. This implies that the net lift given by Eq. (14) does not change significantly with altitude if the helium inside the envelope is free to expand. Introducing B/W, the buoyancy can be easily calculated. When B/W is less than 1.0, it is classified as a lightness condition, whereas when B/W is greater than 1.0, it corresponds to a heaviness condition [17]. Neutral buoyancy is when $B/W = 1.0$.

D. Atmospheric and Jet Stream Modeling

There are two major environmental factors that influence the optimal trajectory of SAP. The first one is atmospheric properties. During the flight, the pressure and density variation at the flight altitude is important, because it affects lift and drag forces. For acquiring such properties, temperature should be calculated first according to its profile over three regions: first, the gradient region with the lapse rate of −0.0065 K/m up to 11 km; next, the isothermal region from 11 to 20 km; and one more gradient region over 20 km with increasing temperature by 1.0 K/m. According to the unique temperature profile along the altitude, the standard atmosphere can be modeled easily as a function of altitude [5].

Apparently, another main influencing factor is jet stream, because its maximum mean velocity is around 40 to 60 m/s in the troposphere of 10–20-km altitude. The jet stream is a narrow, fast, upper atmospheric wind current flowing quasi horizontally at high altitude. The average position of the jet stream changes seasonally, and its winter position tends to be located at a lower altitude and latitude than summertime.

In this paper, statistical meteorological measurement data from 1985 to 2000 are used to develop a jet stream model over the Korean peninsula. The data comprise pressure, temperature, humidity, wind direction, and a wind speed field from 1.5 to 26.5 km. The candidate launch site for the VIA-200 will be located in the southern part of our country, and so the data of the local meteorological observatory are selected. Figure 6 shows maximum, minimum, and average wind

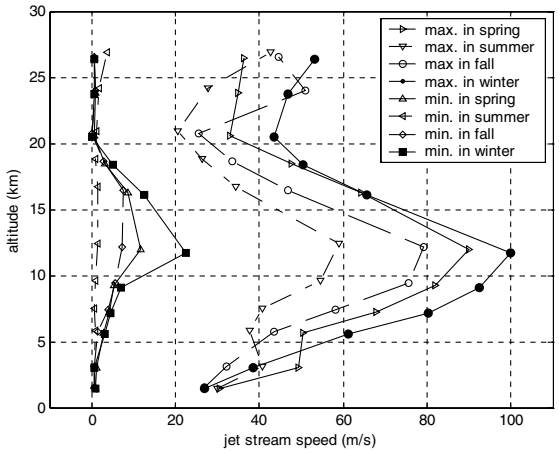

Fig. 6 Statistical data of maximum and minimum velocity of the jet stream in season.

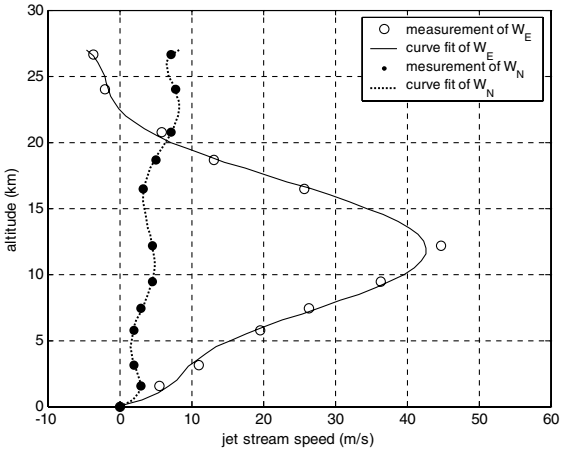

Fig. 7 North and east component of the jet stream velocity in fall.

speeds in each season. As explained previously, the jet stream speed during the winter is more severe than in the summer.

From a practical point of view, the winter is not a good season for launching the SAP, because its maximum jet stream speed is around 40 m/s, even at the staion-keeping altitude of 20 km. Summer is strongly suggested as a candidate season for launching. In this paper, the fall season data are selected for the trajectory optimization problem. The northern and eastern components of jet stream velocity are calculated from the jet stream speed and direction, based on the measurement data, using the following equations:

$$w_E = -w \sin \psi_w, \qquad w_N = -w \cos \psi_w \tag{15}$$

where w represents jet stream speed along the altitude. Fitting the calculated jet stream components data in a seventh-order polynomial, the following final approximations are derived as functions of altitude, as shown in Fig. 7:

$$\begin{aligned} w_E(\bar{h}) &= 3.770\bar{h}^7 - 12.5587\bar{h}^6 - 9.1512\bar{h}^5 + 50.2420\bar{h}^4 \\ &\quad + 6.3696\bar{h}^3 - 73.9562\bar{h}^2 - 4.4017\bar{h} + 42.6254 \\ w_N(\bar{h}) &= 4.5571\bar{h}^7 - 4.8683\bar{h}^6 - 16.180\bar{h}^5 + 12.8161\bar{h}^4 \\ &\quad + 17.7469\bar{h}^3 - 7.6892\bar{h}^2 - 3.3630\bar{h} + 4.5189 \end{aligned} \tag{16}$$

Note that the unit of altitude is in meters, whereas the jet stream speed is in meters per second. The scaling problem arises during the curve fitting, and so the normalization process is applied to improve the accuracy. A normalization approach is to center the data at zero mean and scale it to unit standard deviation using $\bar{h} = (h - \mu_d)/\sigma_d$ with $\mu_d = 12,135$ m and $\sigma_d = 9022$ m, considering the altitude range from 0 to 26 km in 4-km increments.

IV. Optimal Problem Formulation

A. Conversion to Parameter Optimization Problem

The trajectory optimization can be formulated as a dynamic optimization problem, because it is based upon the differential dynamic equations of the vehicle. Consider a system dynamics described by the following nonlinear differential equations:

$$\dot{\boldsymbol{x}}(t) = f[\boldsymbol{x}(t), \boldsymbol{u}(t), t], \qquad \boldsymbol{x}(t_0) = \boldsymbol{x}_0 \text{ is given}, \qquad t \in [t_0, t_f] \tag{17}$$

where $\boldsymbol{x} \in \mathbb{R}^n$, $\boldsymbol{u} \in \mathbb{R}^m$. In this study, $\boldsymbol{x} = [\,V \quad \gamma \quad \psi \quad x_i \quad y_i \quad h]^T$ and $\boldsymbol{u} = [\,T \quad \alpha \quad \phi]^T$, respectively. The main objective of the optimization problem is to find a control input $\boldsymbol{u}$ and a design parameter $\boldsymbol{p} \in \mathbb{R}^p$ that minimize a performance index:

$$J = \varphi[\boldsymbol{x}(t_f), \boldsymbol{u}(t_f), \boldsymbol{p}] \tag{18}$$

which is subjected to initial conditions at time $t = t_0$, terminal conditions at time $t = t_f$, and path constraints during the time

interval $t \in [t_0, t_f]$ [21]:

$$\boldsymbol{\Psi}_E(\boldsymbol{x}_0, \boldsymbol{u}_0, \boldsymbol{p}) = \boldsymbol{0}, \qquad \boldsymbol{\Psi}_I(\boldsymbol{x}_0, \boldsymbol{u}_0, \boldsymbol{p}) \le \boldsymbol{0}, \qquad \boldsymbol{\Psi}_E(\boldsymbol{x}_f, \boldsymbol{u}_f, \boldsymbol{p}) = \boldsymbol{0}$$
$$\boldsymbol{\Psi}_I(\boldsymbol{x}_f, \boldsymbol{u}_f, \boldsymbol{p}) \le \boldsymbol{0}, \qquad \boldsymbol{\Upsilon}[\boldsymbol{x}(t), \boldsymbol{u}(t), \boldsymbol{p}] \le \boldsymbol{0} \tag{19}$$

where $\boldsymbol{\Psi}_E(\cdot)$, $\boldsymbol{\Psi}_I(\cdot)$, and $\boldsymbol{\Upsilon}(\cdot)$ represent the equality, inequality, and path constraints, respectively.

One of the standard approaches for solving this dynamic optimization problem is to convert it into a parameter optimization problem and solve it using an existing nonlinear programming (NLP) tool such as SQP [22]. This well-known approach is categorized as the direct shooting method [6,7]. The direct method has an advantage of not requiring the necessary optimality conditions and adjoint variables [6,7].

The main conversion process is summarized as follows:

1) Divide the time interval into a prescribed number of subintervals t_k ($k = 1, \cdots, N$, $t_1 = t_0$, and $t_N = t_f$), with the times at the ends of subintervals called nodes.

2) The unknown input parameters (control input vector) and design parameters are discretized.

3) The nonlinear differential equations of the optimal control problem are integrated.

4) The nonlinear programming code iterates on the unknown parameters until the boundary conditions and constraints are satisfied. During this process, the fourth-order Runge–Kutta method is employed for numerical integration in this paper. The converted NLP problem [21] is then presented as

$$\boldsymbol{\Theta} = [\boldsymbol{u}_1^T, \boldsymbol{u}_2^T, \boldsymbol{u}_3^T, \cdots, \boldsymbol{u}_N^T, \boldsymbol{p}^T]^T \qquad (\in \mathbb{R}^{m_p}) \tag{20}$$

which attempts to minimize

$$\bar{J}(\boldsymbol{\Theta}) = \varphi(\boldsymbol{x}_N, \boldsymbol{u}_N, \boldsymbol{p}) \qquad (\in \mathbb{R}^1) \tag{21}$$

subject to equality and inequality constraints

$$\boldsymbol{C}_E(\boldsymbol{\Theta}) = \begin{bmatrix} \boldsymbol{\Psi}_E(\boldsymbol{x}_0, \boldsymbol{u}_0, \boldsymbol{p}) \\ \boldsymbol{\Psi}_E(\boldsymbol{x}_f, \boldsymbol{u}_f, \boldsymbol{p}) \end{bmatrix} = \boldsymbol{0} \ (\in \mathbb{R}^{m_E})$$
$$\boldsymbol{C}_I(\boldsymbol{\Theta}) = \begin{bmatrix} \boldsymbol{\Psi}_I(\boldsymbol{x}_0, \boldsymbol{u}_0, \boldsymbol{p}) \\ \boldsymbol{\Upsilon}(\boldsymbol{x}_0, \boldsymbol{u}_0, \boldsymbol{p}) \\ \vdots \\ \boldsymbol{\Upsilon}_N(\boldsymbol{x}_N, \boldsymbol{u}_N, \boldsymbol{p}) \\ \boldsymbol{\Psi}_I(\boldsymbol{x}_f, \boldsymbol{u}_f, \boldsymbol{p}) \end{bmatrix} \le \boldsymbol{0} \ (\in \mathbb{R}^{m_I}) \tag{22}$$

B. Constraints Consideration

For a realistic trajectory optimization problem, details of the constraints and boundary conditions should be defined and examined in consideration of the performance of vehicles and environmental conditions. To achieve the main goal of this study, which is obtaining VIA-200's optimal-ascent trajectories in minimum flight time and/or minimum control energy to the staion-keeping altitude, the concerning performance index is defined by using weighting parameters ξ and η, such that

$$J = \xi \int_{t_0}^{t_f} \mathrm{d}t + \eta \int_{t_0}^{t_f} \frac{1}{2} \|\boldsymbol{u}(t)\|^2 \, \mathrm{d}t \quad \text{or}$$
$$\bar{J}(\boldsymbol{\Theta}) = \xi \sum_{i=1}^{N} \Delta t_i + \eta \sum_{i=1}^{N} \left[\frac{1}{2} \|\boldsymbol{u}_i\|^2 \cdot \Delta t_i \right] \tag{23}$$

As one of the equality constraints, the initial conditions are acquired by assuming a level flight at sea level. Consequently, the trimmed states can be computed from Eq. (9), with the initial flight speed 8.184 m/s, the flight path angle 0 deg, and the heading angle 270 deg.

For terminal conditions, the final staion-keeping horizontal position must maintain minimum deviation from the launch site, and the terminal altitude is 20 km. Also, both γ and ψ must be matched with the initial conditions. It is desired that the VIA-200 should be headed west in its start flying, because the jet stream is blowing from the west. Note that $\psi = 270$ deg is directing west, because ψ is measured positive from the x_h axis (north direction) in the right-hand direction about the z_h axis.

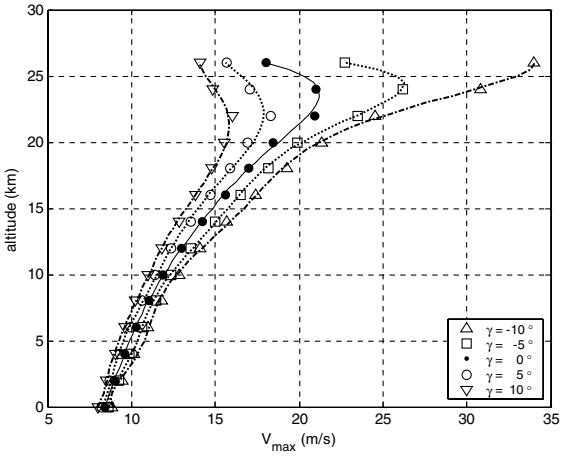

Fig. 8 Maximum flight speed of the VIA-200.

With reference to the path constraints, the admissible flight altitude of the VIA-200 should range from 0 to 24 km of the pressure altitude, based on the design criteria described in Sec. II. The flight speed of the VIA-200 is limited, due to the maximum available power of the propulsion system. Based on this analysis, shown in Fig. 8, the maximum speed $V_{\max} = 30.8$ m/s can be achieved in descending flight, with the flight path angle of -10 deg at the altitude of 24 km.

The climbing performance of the VIA-200 should be the most important consideration when constructing the trajectory. In general, an airship should keep the inner envelope pressure with respect to the atmospheric pressure under climbing or descending path, and so a pressurization control system using an electrical fan and valve is to be equipped. Depending on the given design of the pressurization system and power, the rate of climb $\dot{h}$ should be limited to its maximum capacity. Referring to the flight test results of the VIA-50, the maximum climb rate was estimated as 6.0 m/s. Thus, the upper bound of the SAP is assigned as $\|\dot{h}\| \le 8.0$ m/s. Such an upper bound is considered as a reasonable constraint from the perspective of future technology level.

The control inputs consist of thrust, angle of attack, and bank angle, and control input bounds must be implemented. In practice, the control inputs are normalized for convergence of the solution during the optimization process, and so thrust can be bounded in terms of Tr. Figure 9 presents the lift/drag ratio C_L/C_D of the VIA-

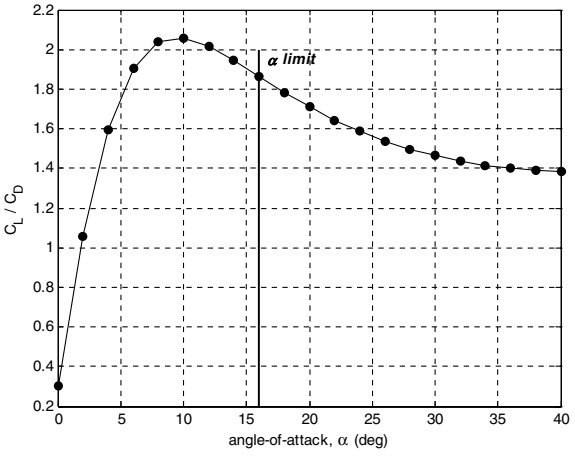

Fig. 9 Range of the angle of attack.

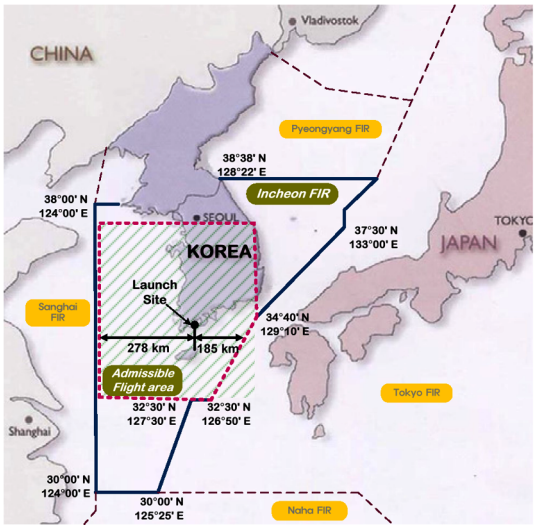

Fig. 10 Admissible flight area according to the flight information region in Korea.

200 versus α, showing that the maximum magnitude is attained at $\alpha = 10$ deg and then it begins falling. Compared with conventional fixed-wing aircraft, its magnitude is small and the slope of the curve is not steep. Furthermore, a control surface effect must be taken into account. Thus, the angle of attack should be bounded at $\|\alpha\| \leq 16$ deg to prevent a stall region of the vertical and horizontal control surfaces, even if there is no stall phenomenon in lift coefficients, as illustrated in Fig. 4. As the last control input bound, a bank angle limit of $\|\phi\| \leq 5$ deg is implemented.

Finally, the airspace limitations should be considered. Because the VIA-200 has low flight speed compared with that of the jet stream, there is a possibility of crossing neighboring countries' territorial airspace. The expected launch site is at 34°32′ N and 127°12′ E, and so the airspace is constrained to 185 km to the east, 278 km to the west, 448 km to the north, and 224 km to the south from the launch site. The admissible flight area is presented in Fig. 10. All of the constraints explained are summarized as follows:

1) The initial conditions at $t = t_0$ are

$$V(t_0) = 8.184 \text{ m/s}, \quad \gamma(t_0) = 0 \text{ deg}, \quad \psi(t_0) = 270 \text{ deg}$$
$$x_i(t_0) = 0 \text{ km}, \quad y_i(t_0) = 0 \text{ km}, \quad h(t_0) = 0 \text{ km} \tag{24}$$

2) The terminal conditions at $t = t_f$ are

$$C_{E,1} = \gamma(t_f) = 0 \text{ deg}, \quad C_{E,2} = \psi(t_f) - 270 \text{ deg} = 0$$
$$C_{E,3} = x_i(t_f) = 0 \text{ km}, \quad C_{E,4} = y_i(t_f) = 0 \text{ km} \tag{25}$$
$$C_{E,5} = h(t_f) - 20 \text{ km} = 0$$

3) The path constraints at time $t_0 < t < t_f$ are

$$C_{I,1} = 0 \text{ km} - h(t) \leq 0, \quad C_{I,2} = h(t) - 24 \text{ km} \leq 0$$
$$C_{I,3} = 0 \text{ m/s} - V(t) \leq 0, \quad C_{I,4} = V(t) - 30.81 \text{ m/s} \leq 0$$
$$C_{I,5} = -8 \text{ m/s} - \dot{h}(t) \leq 0, \quad C_{I,6} = \dot{h}(t) - 8 \text{ m/s} \leq 0$$
$$C_{I,7} = 0 - Tr(t) \leq 0, \quad C_{I,8} = Tr(t) - 1 \leq 0$$
$$C_{I,9} = -16 \text{ deg} - \alpha(t) \leq 0, \quad C_{I,10} = \alpha(t) - 16 \text{ deg} \leq 0$$
$$C_{I,11} = -5 \text{ deg} - \phi(t) \leq 0, \quad C_{I,12} = \phi(t) - 5 \text{ deg} \leq 0$$
$$C_{I,13} = -224 \text{ km} - x(t) \leq 0, \quad C_{I,14} = x(t) - 448 \text{ km} \leq 0$$
$$C_{I,15} = -278 \text{ km} - y(t) \leq 0, \quad C_{I,16} = y(t) - 185 \text{ km} \leq 0 \tag{26}$$

V. Optimal Flight Trajectory of the VIA-200

The numerical solutions are discussed in this section. It is assumed that the VIA-200 is deployed from the ground and it continues to climb up to the mission altitude of 20 km for the staion-keeping mission. Several path constraints defined in the previous section are applied with the governing kinematic and force equations in Eqs. (4) and (9). Relevant modeling for SAP's realistic trajectory optimization was explained in the previous section. As for the numerical solver, the CFSQP algorithm was modified to solve the parameter optimization problem [6,7]. The control variables are throttle, angle of attack, and roll angle, and they are all normalized to facilitate the convergence of numerical solutions. The number of nodes for discretizing the time interval is $N = 1000$, and so the total number of unknown parameters defined in Eq. (20) is $m_p = 3N + 1$, because m_p consists of $\boldsymbol{u} \in \mathbb{R}^3$ and one design parameter of p. As explained in [7], the problem with free final time can be solved by inserting the final time as an additional parameter p. Therefore, the unknown parameters are defined as follows:

$$\Theta = [Tr_1, Tr_2, \ldots, Tr_N, \alpha_{N+1}, \alpha_{N+2}, \ldots, \alpha_{2N}, \phi_{2N+1}, \phi_{2N+2}, \ldots, \phi_{3N}, p]^T \tag{27}$$

The dimensions of relevant vectors introduced in the previous section are $n = 3$, $m = 3$, $p = 1$, $m_p = 3001$, $m_E = 11$, and $m_I = 16N = 16,000$. The optimization process is terminated if all of the terminal conditions in Eq. (25) are satisfied within numerical error tolerances. The terminal error criteria are $\|e_x\|^2$, $\|e_y\|^2$, and $\|e_z\|^2 \leq 10^{-2}$ m for the geostationary position and $\|e_\gamma\|^2$ and $\|e_\psi\|^2 \leq 10^{-2}$ deg for angle, respectively.

A. Cases 1 and 2: Minimum-Time Trajectories

Case 1 presents the minimum-time flight trajectory obtained by solving the problem with $\xi = 1$ and $\eta = 0$ in the performance index of Eq. (23), and case 2 adds the jet stream effect to case 1. The resultant trajectories are of great importance, because they demonstrate the effects of the jet stream. As the outcome of the optimization presented in Figs. 11–15, the terminal flight path angle satisfies $\gamma_f = 0$ deg and the heading angle $\psi_f = 270$ deg in Eq. (25). It also implies that the solution meets the final position requirement of $x_f = 0$ km, $y_f = 0$ km, and $h_f = 20$ km within the error tolerance.

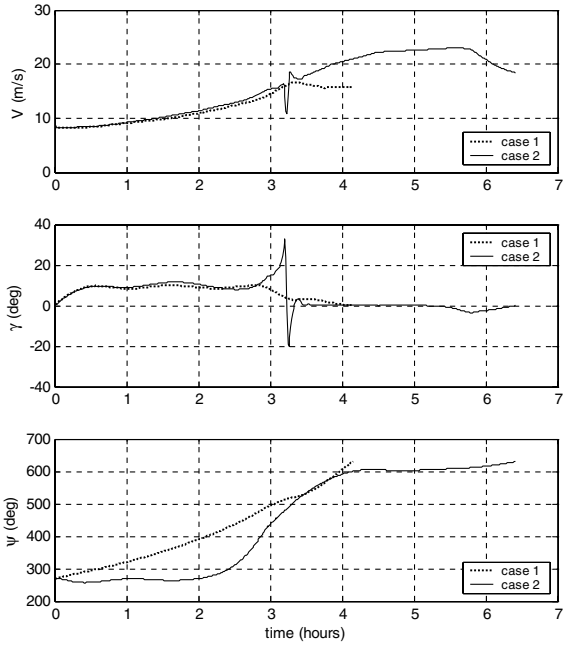

Fig. 11 State histories for cases 1 and 2.

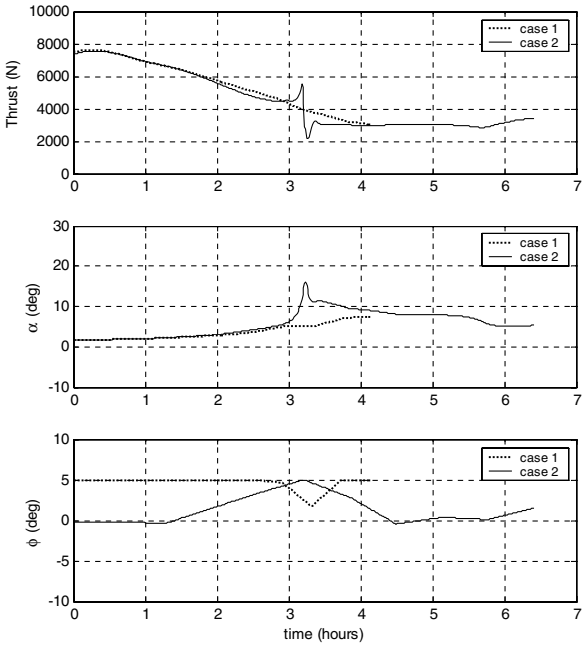

Fig. 12 Control input histories for cases 1 and 2.

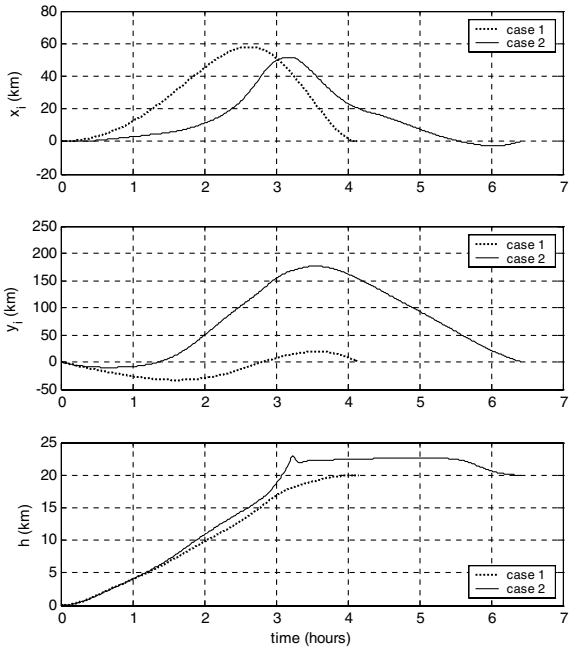

Fig. 13 Position histories for cases 1 and 2.

For case 1, the altitude increases monotonically in proportion to the flight speed. This result is consistent with that of [5]. It keeps exerting full thrust with the maximum climbing flight speed until about $t = 2.78$ h, and then it increases a little sharply to reduce the flight path angle to meet the terminal constraint of 0 deg. The resultant trajectory is in a helix shape (Fig. 15) and is inside 60 km for the x_i axis (north) and ± 40 km for the y_i axis (east).

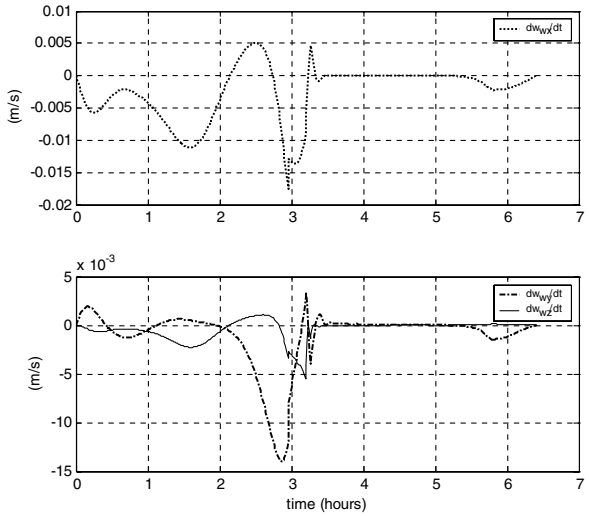

Fig. 14 Wind variation histories for case 2.

For case 2, the VIA-200 cannot overcome the strong wind speed until it reaches the altitude of 22 km. It flew away to the east, because the jet stream is so strong. As shown in Fig. 7, the east-wind speed of the jet stream is peaked at the altitude of 12–13 km and then becomes weaker above that altitude. Thus, the airship attempts to maintain its heading to the west by relying on full thrust. After it approaches the altitude of 15 km, it starts a turning flight to reach the final destination. It keeps the level flight at the altitude of 22 km and then descends to the desired final altitude. Figures 11 and 12 present the state and control histories versus flight time, and Fig. 13 shows the position histories of each axis. From the results, the VIA-200 drifts approximately 177 km to the east and 52 km to the north, as presented in Fig. 13. However, the position is inside the airspace boundary. During the flight, the flight speed and path angle show fluctuation at around $t = 3.2$ h. This is due to the wind speed variation along the altitude, as shown in Fig. 14. Flight speed is affected by the $\dot{w}_{wx}$ term, and the flight path angle is affected by $\dot{w}_{wy}$ and $\dot{w}_{wz}$, defined in the force equation of Eq. (9). This phenomenon occurs markedly during the turning flight condition. Three-dimensional minimum flight time trajectories for case 2 in Fig. 15 show a comparison with case 1. Based on the results, it is confirmed that the optimal solution meets all of the equality and inequality constraints.

Table 3 summarizes the results of the trajectories generated. The terminal time for case 1 is $t_f = 4.15$ h and is $t_f = 6.42$ h for case 2. Clearly, the terminal time for case 2 is longer than for case 1. It is worthwhile to note that additional control energy is required 61.5% more, with a 54.7% increase in flight time, in contrast to case 1 under the no-jet-stream condition.

B. Cases 3 and 4: Minimum-Energy Trajectory Under Jet Stream

In this example, the minimum-energy trajectories are examined under the jet stream condition. It is infeasible to augment the control energy term in the performance index, except the minimum flight time, because the fixed final horizontal position and free terminal flight time are now considered. Thus, trajectories are constructed by solving the minimum control energy with the minimum flight time with $\xi = 1$ and varying the energy-weighting parameter η in Eq. (23). The trajectory may depend on the selection of the weighting parameters. In this example, η is set to 1 or 100 with case 3 and case 4,

Table 3 Comparison of optimal trajectories results

Case no.	Cost function	Weighting	Jet stream	Terminal time, t_f	Cost of energy
1	Min time	$\xi = 1$ and $\eta = 0$	——	4.15 h	0.62
2	Min time	$\xi = 1$ and $\eta = 0$	○	6.42 h	1.0
3	Min time + min energy	$\xi = 1$ and $\eta = 1$	○	8.67 h	0.93
4	Min time + min energy	$\xi = 1$ and $\eta = 100$	○	10.27 h	0.84

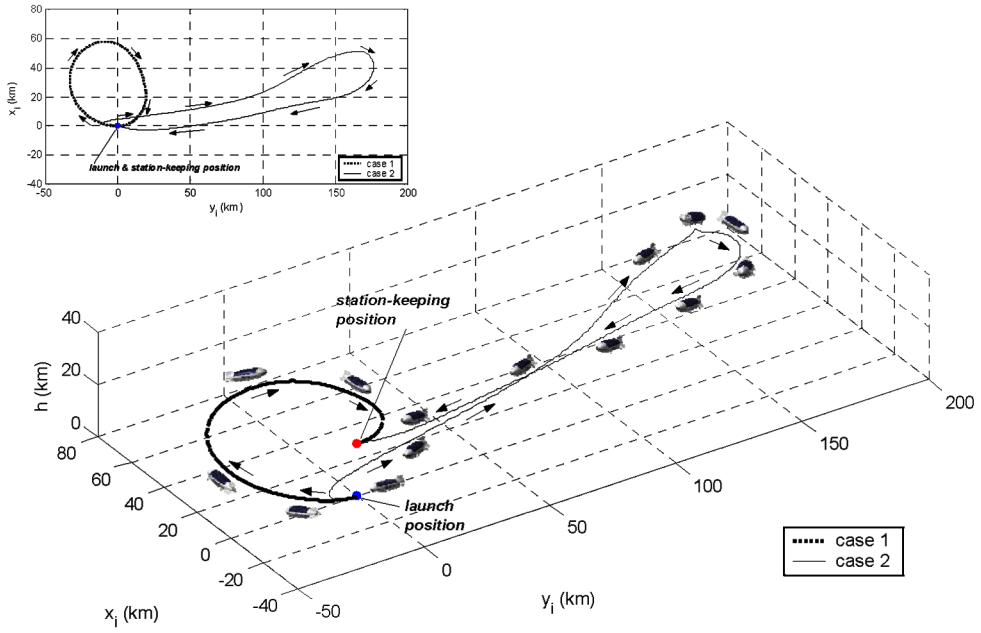

Fig. 15 Three-dimensional optimal trajectories for cases 1 and 2.

respectively. The final solutions are compared with the minimum-time solution to case 2 ($\xi = 1$ and $\eta = 0$). Figures 16–18 present the state, control, and position histories, respectively. Specifically, the climb and descent rates are critical constraints, as explained earlier. Figure 19 presents rate histories versus time, and they stay less than the specified constraints on $\dot{h}$. In addition, two-dimensional and three-dimensional trajectories are displayed in Figs. 20 and 21.

Similar to the previous cases of minimum flight time trajectory, the numerical solutions sufficiently satisfy all of the path constraints of $\gamma_f = 0$ deg and $\psi_f = 270$ deg. The VIA-200 arrives at the terminal positions of $x_f = 0$ km, $y_f = 0$ km, and $h_f = 20$ km almost exactly.

Control energy decreases correspondingly as the weighting parameter increases from 1 to 100, and the terminal time t_f also increases. The final outcome indicates that t_f is 8.67 h for case 3 ($\eta = 1$) and 10.27 h for case 4 ($\eta = 100$). Apparently, the radius of turning flight, after weakening of the jet stream, seems to become wider than with case 2. The maximum range of x_i and y_i deviations from the launch position are about 55 and 184 km, respectively, and so the airspace boundary limit is not violated, as confirmed from Fig. 18. Obviously, the reason the deviation in the x_i position increases over 20 km is because the northern speed component of the jet stream tends to increase along the altitude, as shown in Fig. 7. Thus, decreasing control energy enlarges the deviation of the x_i position and causes the flight time to increase. The heading angle shows a similar tendency to keep maintaining the west direction until the eastern component of the jet stream speed becomes weaker, but the time of starting the turning flight is different from each other. More maneuver time is expected as the weighting η becomes large.

From an energy-saving standpoint, the amount of control energy involved for case 3 ($\eta = 1$) is reduced to 6.7% and reduced to 15.8% for case 4 ($\eta = 100$), compared with the minimum-time trajectory of case 2, as summarized in Table 3. On the other hand, the flight time increases 35.0% in case 3 ($\eta = 1$) and 60.1% in case 4 ($\eta = 100$), respectively. The amount of decreased energy is not much over the

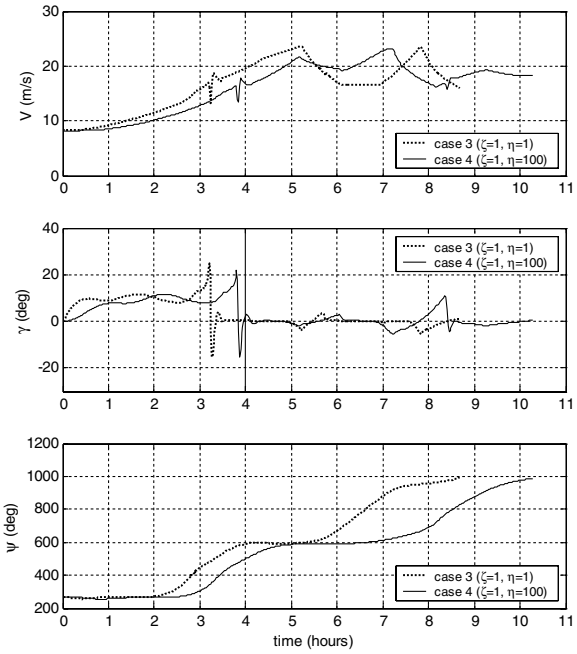

Fig. 16 State histories for cases 3 and 4.

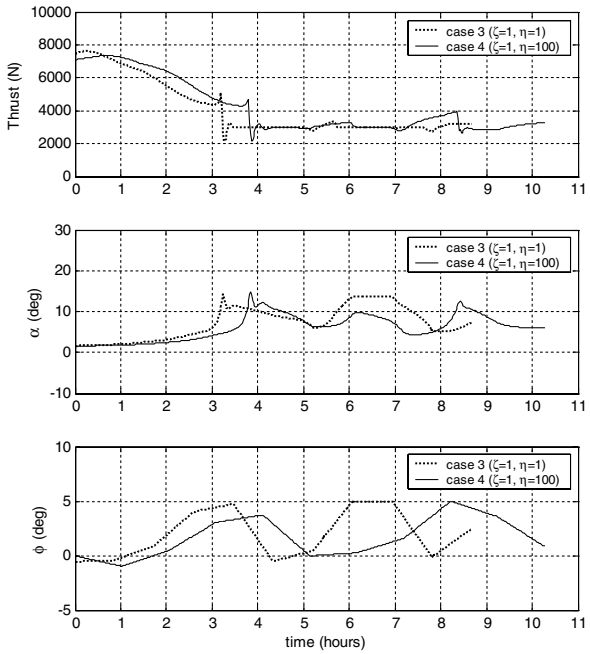

Fig. 17 Control input histories for cases 3 and 4.

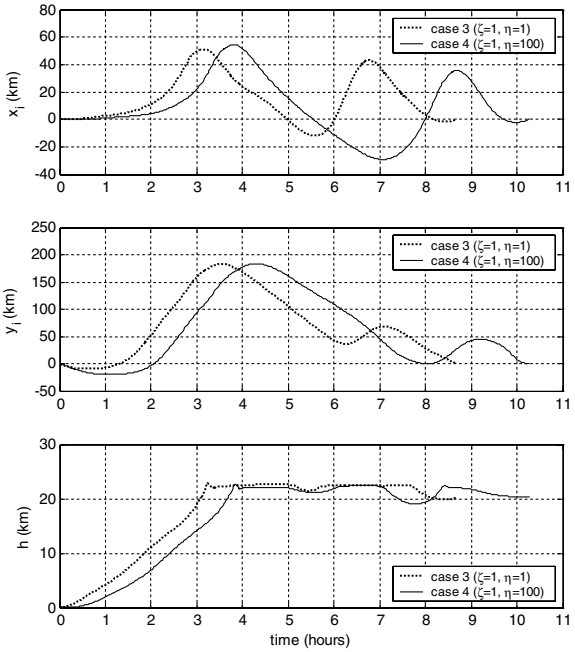

Fig. 18 Position histories for cases 3 and 4.

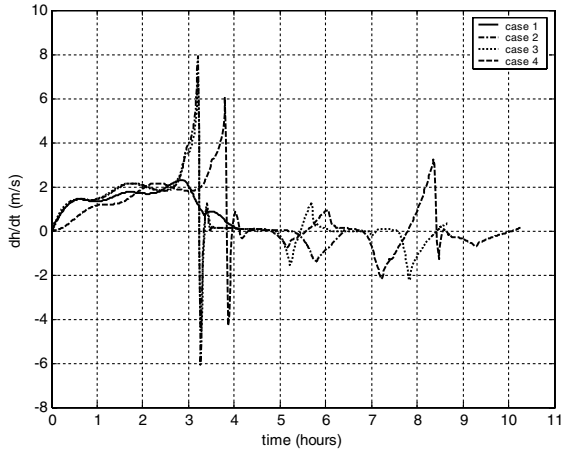

Fig. 19 Climb and descent rate histories.

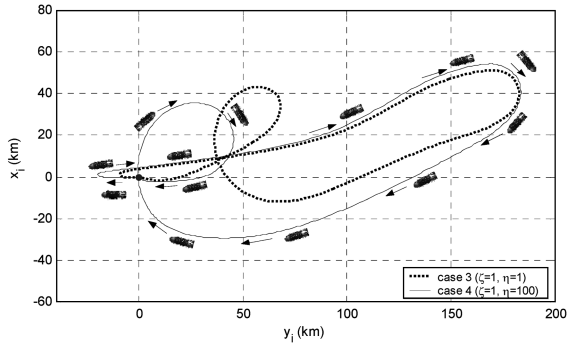

Fig. 20 Two-dimensional horizontal position histories for cases 3 and 4.

flight time increase and, consequently, it may not be a large benefit in saving energy. Based on such results, it is concluded that the minimum-time flight trajectory for the VIA-200 is recommended under the real flight environments such as the jet stream. Judging from the aspect of trajectory deviation with respect to the airspace constraints, the trajectory of case 3 ($\eta = 1$) is preferred over case 4 ($\eta = 100$) because it covers the shortest distance. The optimal trajectories obtained in this paper will be used as baseline information and applied to a trajectory-tracking controller design in the future.

VI. Conclusions

This paper is concerned with the optimal trajectory generation for the SAP, especially the ascent flight trajectory synthesis to a staion-keeping position with and without jet stream. The SAP arrived at the given final position of $x_f = 0$ km, $y_f = 0$ km, and $h_f = 20$ km, successfully satisfying the prescribed geometric boundary constraints.

With no jet stream condition (case 1), the trajectory designed turned out to be a helix shape and the altitude increased monotonically in proportion to the flight speed of the SAP. The resultant trajectory was inside ± 40 km for the y_i axis (eastern direction) and 60 km for the x_i axis (northern direction). When encountering the jet stream (case 2), the airship was not able to overcome the strong jet stream and slipped away to the east, trying to maintain its heading to the west by exerting full thrust. After the jet stream speed becomes weaker, the SAP started the turning flight to approach the terminal destination. However, the overall airship trajectory stayed inside the designated airspace boundaries. The

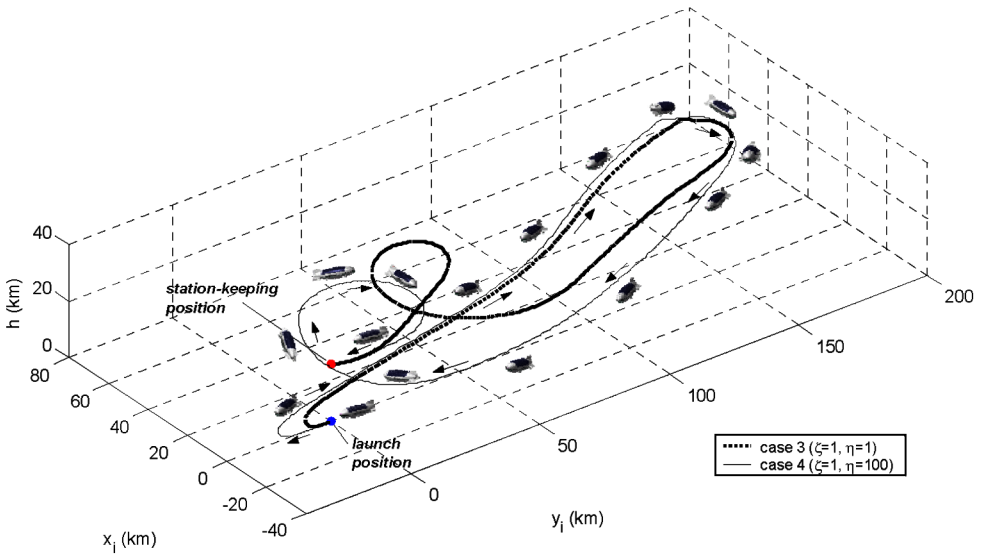

Fig. 21 Three-dimensional optimal trajectories for cases 3 and 4.

terminal time with jet stream (case 2) increased 54.7%, in contrast to a 61.5% energy increase with the no-jet-stream case (case 1). As for the minimum-energy trajectories, the amount of used control energy was reduced to 6.7% for case 3 (weighting $\eta = 1$) and 15.8% for case 4 (weighting $\eta = 100$) over the minimum-time trajectory of case 2 (weighting $\eta = 0$). The amount of energy saved was not that remarkable relative to the flight time and so it may not be a significant benefit from the energy-saving standpoint. Therefore, it is concluded that the minimum-time flight trajectory for the VIA-200 is recommended under a real flight scenario under jet stream. This means that the SAP has no available power, due to the low flight performance, in contrast to its huge size and heavy weight.

Finally, the main contributions of this paper are attributed to accommodating the realistic flight conditions and path constraints as accurately as possible. Furthermore, corresponding three-dimensional flight trajectories by an optimization technique are constructed, which can be used for a feedback-tracking controller design in actual implementation.

Acknowledgments

The authors would like to thank the Korea Ministry of Commerce, Industry, and Energy for their support of this project and for the permission to publish this work.

References

[1] Colozza, A., "Initial Feasibility Assessment of a High Altitude Long Endurance Airship," NASA CR-2003-212724, Dec. 2003.

[2] Eguchi, K., and Yokomaku, Y., "Overview of Stratospheric Platform Airship R&D Program in Japan," *Proceedings of the 14th Lighter-Than-Air Technical Committee Convention and Exhibition*, AIAA, Reston, VA, 2001.

[3] Bestaoui, Y., and Hamel, T., "Dynamic Modeling of Small Autonomous Blimp," *Proceedings of the International Symposium on Methods and Models in Automation and Robotics*, Wydawnictwo Uczelniane Politechniki Szczecinskiej, Szczecin, Poland, Aug. 2000, pp. 579–584.

[4] Hima, S., and Bestaoui, Y., "Motion Generation on Trim Trajectories for an Autonomous Underactuated Airship," *Proceedings of the 4th International Airship Conference*, Airship Association, Kent, England, U.K., 2002.

[5] Zhao, Y. J., Garrard, W. L., and Mueller, J., "Benefits of Trajectory Optimization in Airship Flights," *Proceedings of the 3rd AIAA Unmanned Unlimited Technical Conference*, AIAA, Reston, VA, 2004.

[6] Betts, J. T., "Survey of Numerical Methods for Trajectory Optimization," *Journal of Guidance, Control, and Dynamics*, Vol. 21, No. 2, 1998, pp. 193–205.

[7] Hull, D. G., "Conversion of Optimal Control Problems into Parameter Optimization Problems," *Journal of Guidance, Control, and Dynamics*, Vol. 20, No. 1, 1997, pp. 57–60.

[8] Lawrence, C., Zhou, J. L., and Tits, A. L., "User's Guide for CFSQP (C-code for Feasible Sequential Quadratic Programming) Ver. 2.5: A C-Code for Solving (Large Scale) Constrained Nonlinear (Minimax) Optimization Problems, Generating iterates Satisfying All Inequality Constraints," Univ. of Maryland, College Park, MD, 1997.

[9] Lee, Y. G., Kim, D. M., Lee, H. C., and Yeom, C. H., "Concept Design of a Stratospheric Airship," *Proceedings of the Korean Society for Aeronautical and Space Sciences Fall Conference*, Korean Society for Aeronautical and Space Sciences, Seoul, Republic of Korea, Nov. 2003, pp. 445–449 (in Korean).

[10] Miele, A., Wang, T., and Melvin, W. W., "Optimal Take-Off Trajectories in the Presence of Windshear," *Journal of Optimization Theory and Applications*, Vol. 49, No. 1, 1986, pp. 1–45.

[11] Psiaki, M. L., and Stengel, R. F., "Optimal Aircraft Performance During Microburst Encounter," *Journal of Optimization Theory and Applications*, Vol. 14, No. 2, 1991, pp. 440–446.

[12] Thomasson, P. G., "On Calculating the Motion of a Vehicle in a Moving Fluid," *Proceedings of the 3rd International Conference on Nonlinear Problems in Aviation and Aerospace*, European Conference Publications, Cambridge, England, U.K., 2001, pp. 645–652.

[13] Feldman, M. A., "Efficient Low-Speed Flight in a Wind Field," M.S. Thesis, Virginia Polytechnic Inst. and State Univ., Blacksburg, VA, July 1996.

[14] Khoury, G. A., and Gillet, J. D., *Airship Technology*, Cambridge Univ. Press, New York, 1999.

[15] Jang, B. H., and Park, Y. M., "Extension of Aerodynamic Database of the Stratospheric Airship by Using CFD Results," Korea Aerospace Research Institute, Technical Rept. KARI-AD-TN-2004-001, Mar. 2004 (in Korean).

[16] Sighard, F. H., *Fluid Dynamic Drag: Practical Information on Aerodynamic Drag and Hydrodynamic Resistance*, Hoerner Fluid Dynamics, Brick Town, NJ, 1965.

[17] Gomes, S. B. V., "An Investigation of the Flight Dynamics of Airships with Application to the YEZ-2A," Ph.D. Dissertation, College of Aeronautics, Cranfield Univ., Cranfield, England, U. K., Oct. 1990.

[18] Goineau, F., and Cook, M. V., "The Stability and Control Characteristics of the Neutrally Buoyant Non-Rigid Airship," College of Aeronautics, Cranfield Univ., Rept. 9911, Cranfield, England, U.K., Aug. 1999.

[19] Lamb, H., "The Inertia Coefficient of an Ellipsoid Moving in Fluid," Aeronautical Research Committee, Reports and Memoranda 623, Oct. 1918.

[20] Ok, H. N., Jang, B. H., Lee, Y. G., Lee, S. J., and Lee, J. W., "Calculation of the Added Mass of an Airship," Korea Aerospace Research Inst., Technical Rept. KARI-AD-TM-2002-009, May 2002 (in Korean).

[21] Yokoyama, N., and Suzuki, S., "Modified Genetic Algorithm for Constrained Trajectory Optimization," *Journal of Guidance, Control, and Dynamics*, Vol. 28, No. 1, 2005, pp. 139–144.

[22] Dachwald, B., "Low-Thrust Trajectory Optimization and Interplanetary Mission Analysis using Evolutionary Neurocontrol," Ph.D. Dissertation, Univ. der Bundeswehr München, Munich, Germany, Apr. 2004.